



Effects of solution conductivity on macropore size dynamics in electroporated lipid vesicle membranes

E. Sabri^{a,b}, M. Aleksanyan^{b,c}, C. Brosseau^{a,*}, R. Dimova^b

^a Univ Brest, CNRS, Lab-STICC, CS 93837, 6 avenue Le Gorgeu, 29238 Brest Cedex 3, France

^b Max Planck Institute of Colloids and Interfaces, Science Park Golm, 14476 Potsdam, Germany

^c Institute for Chemistry and Biochemistry, Freie Universität Berlin, Takustraße 3, 14195 Berlin, Germany

ABSTRACT

Using fast imaging microscopy, we investigate in detail the expansion of micron-sized pores occurring in individual electroporated giant unilamellar vesicles composed of the phospholipid 1-palmitoyl-2-oleoyl-sn-glycero-3-phosphocholine (POPC). To infer pore dynamics on the electrodeformed and electropermeabilized vesicles, we develop a computational approach and provide for the first time a direct evidence of quantitative agreement between experimental data and the well-established theoretical prediction of Smith, Neu and Krassowska (SNK). The analysis we describe also provides an extension to the current theoretical literature on how the conductivity ratio of the internal and the external vesicle solution plays a determinant role in the definition of the electrical force driving pore expansion kinetics.

1. Introduction and motivation

Cell electropermeabilization (EP) sets the basis of a number of novel therapeutic strategies, including electrochemotherapy and tumor ablation, drug and gene delivery and cell transfection, to mention a few. These applications motivate the current approach in understanding the EP mechanisms of biological cells and lipid vesicles [1–23]. In these settings, there has been a longstanding debate over the mechanism of pore opening and expansion across cell membranes and/or lipid bilayer. Strong electric fields can trigger phase transitions in phospholipid bilayers and lead to the formation of hydrophilic aqueous pores. However, despite the large amount of work dedicated to set solid theoretical groundings to vesicle and lipid bilayers [24–27] the precise physical mechanisms underlying the generation and expansion of these local defects remain an open question. This challenge is further compounded by the current lack of knowledge of the role of the membrane solution environment which eventually impacts significantly pore nucleation and expansion processes in vesicle and cell membranes [13–14]. In particular, the role of conductivity conditions across the membrane has not been resolved even though conductivity asymmetry is inherent to plasma membranes. In general terms, vesicle membranes can be treated as incompressible fluid interfaces and have significant promise as an arena for investigating multiscale and multiphysics cell membrane EP models. Additionally, there does seem to be (at least) a consensus that the pore size and transmembrane potential, V_m , are two critical variables

in determining EP dynamics, but little is known about the contribution from each cue individually, see e.g. Refs. [13–14]. Current strategies for visualizing the time-dependent behavior of individual electropores in vesicles rely on detecting the dynamics of solute flow between the internal and external volumes and imaging the membrane itself [17–23,28–33], or using optical single-channel recording and fluorescence imaging of bilayers [11].

In light of the above, this work considers a tractable geometric configuration of lipid vesicles for which the electrodeformation (ED) and electroporation phenomena can be simultaneously studied. For this purpose, our analysis is based on the computation of the Maxwell stress tensor (MST) to evaluate the electromechanical forces that induce both membrane deformation [34] and expansion of embedded pores [15]. On the experimental side, the electropore expansion velocity is characterized by studying the dynamics of solute flow between the internal and external volumes of giant unilamellar vesicles composed of POPC. We find that the conductivity ratio of the inside and the outside vesicle solution impacts significantly the expansion velocity of a macropore occurring in electrodeformed and electropermeabilized vesicles. We provide both numerical and analytical support to these findings which are in quantitative agreement with our experimental results. The electrical force needed to expand a transient macropore is computed as a function of the local transmembrane potential and is compared with the experimental data of pore expansion velocities when the conductivity ratio of the internal and external vesicle solutions is varied over two

* Corresponding author.

E-mail address: brosseau@univ-brest.fr (C. Brosseau).

<https://doi.org/10.1016/j.bioelechem.2022.108222>

Received 30 May 2022; Received in revised form 29 July 2022; Accepted 1 August 2022

Available online 3 August 2022

1567-5394/© 2022 Elsevier B.V. All rights reserved.

orders of magnitude. We find that the quadratic dependence of the electric force expanding the pore on the transmembrane potential, V_m is conserved as in the Smith, Neu and Krassowska (SNK) model [15]. On the numerical side, we use finite element simulations in order to quantify the electromechanical behavior of electropermeabilized lipid vesicle membranes [34–36].

2. Background

First theories of lipid membrane electrical breakdown have described the EP phenomena as a stochastic process during which structural defects, presented as aqueous pores [26], form in the membrane when subjected to a sufficiently high transmembrane potential [24–26,37]. Under such steady transmembrane potential, and based on membrane free energy computations, pore nucleation and expansion dynamics were suggested to follow a two-stage process: first nucleating as small cylindrical non conducting pores that expand in the membrane, then becoming conductive pores as they exceed a threshold size (roughly 0.5 nm) as a result of their expansion. This expansion process would eventually result in membrane rupture, characterized by an increase in membrane conductivity by several orders of magnitude [24–26,37]. In these settings, a theoretical description of the EP phenomena was proposed in [26] based on thermodynamics and in which the overall pore population obeys the Smoluchowski equation.

$$\frac{\partial n(r,t)}{\partial t} = D \frac{\partial}{\partial r} \left(\frac{\partial n(r,t)}{\partial r} + n(r,t) \frac{U(r, V_m)}{kT} \right) \quad (1)$$

Here $n(r, t)$ denotes the pore density distribution function, where the number of pores per unit area with a size comprised between r and $r + dr$ is $n(r, t)dr$ [26], D is the diffusion coefficient of pore radius in the r space [26], k is the Boltzmann constant, T is the absolute temperature, t represents time, and $U(r, V_m)$ represents the shift in membrane free energy due to the presence of a pore in the membrane, defined as.

$$U(r, V_m) = -2\pi\gamma + (CV_m^2 + 2\pi\sigma)r \quad (2)$$

where γ , C and σ respectively account for pore edge tension, membrane capacitance per unit area and lipid-water interfacial surface tension [26]. It is also important to notice that Eq. (1) has no analytical solution, and therefore the density distribution of pores in the membrane must be solved numerically [3,27,38]. In addition, the large computational time required for solving Eq. (1) on tractable space and time scales constitute serious drawbacks [38]. To tackle these issues, Neu and Krassowska conducted a thorough analysis in [38] and proposed an asymptotic model to the one presented above, which simplifies the partial differential equation (PDE) of Eq. (1) in two independent ordinary differential equations to describe the time evolution of pore density and pore radii.

$$\frac{dN}{dt} = \alpha \exp(V_m^2/V_{EP}^2) \left(1 - \frac{N}{N_0 \exp(qV_m^2/V_{EP}^2)} \right) \quad (3)$$

and

$$\frac{dr}{dt} = \frac{D}{kT} U(r, V_m). \quad (4)$$

Here N is the pore density, α and q are pore creation rate constants, V_{EP} is the electroporation threshold transmembrane potential and N_0 is the initial number of defects [38]. The expression $U(r, V_m)$ for conducting pores ($r > 0.5$ nm) has been extensively debated in the literature, with particular emphasis on the definition of the energy term related to the induced transmembrane potential V_m [15,25–27,37]. From the perspective of today's understanding, the approach of SNK [9], which consisted in defining the V_m related energy term from the integration of the electric stresses (MST) over the internal boundaries of a toroidal pore [15], has been by far the most reemployed numerical model for cell membrane EP simulation over the past two decades [4–5,10,38–49]. An important remark here is that imbalances in the

conductivities of media surrounding the membrane were neglected, i.e., only the case $\Lambda = 1$ was investigated in the SNK model [9], while the vast majority of membrane EP simulation studies have focused their efforts on modeling the response of systems showing conductivity imbalances of one order of magnitude between the media surrounding the membrane [4–5,10,38–49]. In the SNK model, $U(r, V_m)$ is defined as.

$$U(r, V_m) = \sum_{i=1}^4 U_i = V_m^2 f_{SNK}(r) + \frac{4\beta}{r} \left(\frac{r^*}{r} \right)^4 - 2\pi\gamma + 2\pi\sigma_{eff}r \quad (5)$$

Here $f_{SNK}(r)$ represents a force per unit square voltage [15], β denotes the steric repulsion energy, r^* is the minimum pore radius, and finally, $\sigma_{eff} = 2\sigma' - \frac{2\sigma' - \sigma_0}{(1 - A_p/A)^2}$ is the effective tension of the porated membrane felt by the pore of radius r [50], where A_p and A correspond to the area occupied by the pores and the total membrane area, with σ' and σ_0 defined in Table 1.

The first term of Eq. (2) accounts for the electric force induced by the local value of V_m ; the second represents the steric repulsion of lipid heads, the third, for the edge tension opposing the expansion of the circumference of the pore, and the fourth introduces the surface tension of the membrane [15,38]. Here, we reproduce the numerical method of SNK and extend their model to compute the V_m dependent energy term of Eq. (5) as a function of Λ . In the SNK model, the first term of Eq. (5) takes the form [15].

$$f_{SNK}(r) = F_{max} \frac{r + r_1}{r + r_2} \quad (6)$$

This expression was obtained by SNK as a phenomenological approximation of their numerical computations where F_{max} is the maximal radial force per unit squared Volt, and r_1 and r_2 are two constants [15]. Here, we derive a Λ dependent extension of their model, also based on a similar approximation of our numerical results which has a different analytical expression, namely.

$$f_{\Lambda} = F_{max}(r + r_1) \left(\frac{1}{r + r_2} - \frac{\chi}{r + r_3} \right) \quad (7)$$

where F_{max} , r_1 , r_2 , r_3 and χ are constants which depend only on Λ (discussed below and summarized in Table 2).

Fig. 1 compares the magnitude of all the energy contributions U_i of

Table 1

A summary of the parameters used in the computational model for producing the specified figures.

Parameters	Notation	Numerical value	Fig.	Ref.
Membrane total thickness	d_m (m)	3.70×10^{-9}	1,2,6	[17]
Membrane dielectric thickness	d_{me} (m)	2.71×10^{-9}	6	[17]
Internal medium permittivity	$\epsilon_0 \epsilon_c$ (Fm ⁻¹)	7.08×10^{-10}	1	[15]
Internal medium conductivity	λ_{in} (Sm ⁻¹)	4.4×10^{-4} - 6.2×10^{-3}	1	this work
Membrane permittivity	$\epsilon_0 \epsilon_m$ (Fm ⁻¹)	1.77×10^{-11}	1,6	[15]
Membrane conductivity	λ_m (Sm ⁻¹)	1×10^{-11}	1	[51]
External medium permittivity	$\epsilon_0 \epsilon_e$ (Fm ⁻¹)	7.08×10^{-10}	1	[15]
External medium conductivity	λ_{ext} (Sm ⁻¹)	4.3×10^{-4} - 5.6×10^{-3}	1	this work
Temperature	T (K)	300	5	[51]
Diffusion coefficient for pore radius	D (m ² /s)	5×10^{-14}	5	[51]
Initial surface tension	σ_0 (N/m)	10^{-6}	5	[51]
Steric repulsion energy	β (J)	1.4×10^{-19}	5	[51]
Pore edge tension	γ (N)	2.4×10^{-11}	5	[51]
Energy of hydrocarbon-water interface per unit area	σ' (N/m)	2×10^{-2}	5	[51]
Minimum size of hydrophilic pore at $V_m = 0$ V	r^* (m)	0.51×10^{-9}	5	[51]

Table 2

Fit parameters used for the electric force contribution in $U(r, V_m)$, i.e. $F_p = V_m^2 F_{\max} \left(\frac{1}{r+r_1} - \frac{\chi}{r+r_3} \right)$, as a function of the conductivity ratio Λ . Here, the notation $\{i;1/i\}$ means that $f_\Lambda \equiv f_{1/\Lambda}$.

Λ	$F_{\max}(\text{nN}/\text{V}^2)$	$r_1(\text{nm})$	$r_2(\text{nm})$	$r_3(\text{nm})$	χ
1 (SNK)	0.69	0.23	1.18	0	0
{2;1/2}	1.008	0.242	1.221	1.828	0.399
{3;1/3}	1.599	0.207	1.179	1.544	0.680
{4;1/4}	1.806	0.179	1.079	1.405	0.758
{5;1/5}	1.930	0.157	0.994	1.291	0.803
{6;1/6}	2.186	0.142	0.934	1.183	0.846
{7;1/7}	2.387	0.130	0.880	1.097	0.873
{8;1/8}	2.412	0.121	0.829	1.032	0.887
{9;1/9}	2.356	0.113	0.781	0.980	0.893
{10;1/10}	2.373	0.107	0.744	0.931	0.902

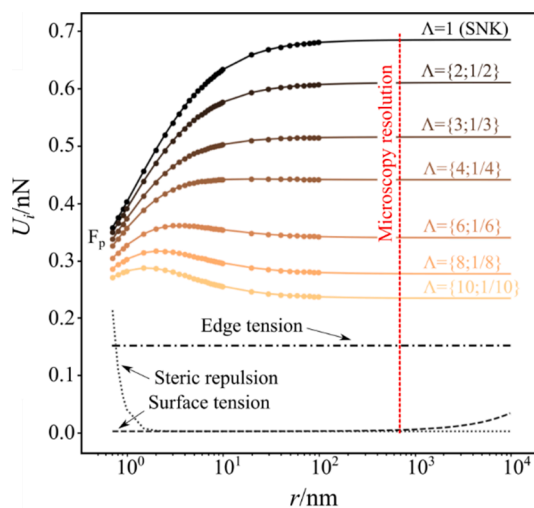


Fig. 1. The predicted change in the four contributions of the force acting on the pore $U(r, V_m = 1V)$ as a function of pore radius for different values of the electrical conductivity ratio Λ of the inside and the outside vesicle solution. F_p denotes the electromechanical force, i.e. the V_m dependent contribution to the $U(r, V_m = 1V)$ energy term. Note that for the electric force $\{i;1/i\}$ means that $f_\Lambda \equiv f_{1/\Lambda}$. The parameterized analytic function $f_\Lambda(r)$ (solid lines) are shown to match well with the numerical solution (solid symbols). For this calculation we assume $\sigma_{\text{eff}} = 10^{-6} \text{N/m}$ and $\gamma = 24 \text{pN}$. The vertical red dotted line represents the limit of our experimental resolution (values of r below this limit are not detected experimentally).

Eq. (5) which are plotted as a function of pore radius, where simulation data points are compared with Eq. (7).

The curve $\Lambda = 1$ (SNK) shows the match between our results and the ones from the SNK model. It is also discernible that the V_m dependent component dominates over the other contributions in the entire range of r investigated, where a variation of one order of magnitude of the value of Λ impacts the magnitude of the V_m dependent component of $U(r, V_m)$ up to a factor 3. Consequently, the combination of Eqs. (4) and (7) suggest a dependence of pore expansion dynamics on conductivity imbalances between membrane surrounding media. Table 2 lists the material properties for cells deduced from consolidated literature data to obtain Fig. 1, and includes details of the numerical method used to compute f_Λ which are completed by Fig. 3.

3. Methods

Before proceeding with our method for inferring the electrical force on a macropore, we pause to discuss how the experimental results of this study should be interpreted in the light of previous work dealing with

the electropermeabilization of giant unilamellar vesicles. Then, we describe the computational procedure for assessing the macropore size dynamics in electropermeabilized vesicles.

3.1. Vesicle preparation, pulse application and resolving the pore dynamics with video microscopy

Giant unilamellar vesicles (GUVs) of palmitoyl-2-oleoyl-sn-glycero-3-phosphocholine (POPC) (Avanti Polar Lipids, Alabaster, AL) were prepared by using the electroformation method [52–53], for which $10 \mu\text{L}$ of a 4mM of lipid solution prepared in chloroform is spread on the surfaces of a pair of indium tin oxide-coated, conductive glasses (Delta technologies Lt., Germany). Then, the glasses were kept in desiccator for 2 h to remove all traces of the organic solvent. The two glasses were then placed with their conductive sides facing each other and separated by a 2 mm-thick Teflon frame to form a chamber. The chamber was filled with a 200mM sucrose (Merck, Germany) containing NaCl at concentrations up to 1mM (Merck, Germany) depending on the desired internal vesicle conductivity. The chamber was then connected to a function generator (Agilent, Germany) and an alternating current (AC) of 1V with a 10Hz frequency was applied for 1 h. After harvesting the vesicle solution from the electroswelling chamber, it was 10-fold diluted in 200mM of glucose solution (Merck, Germany). The external solution also contained 0 and 1mM NaCl to adjust the desired external conductivity. We note that the sugar asymmetry between the interior and the exterior of the vesicle enhances the optical contrast of phase contrast images due to refractive index difference of glucose and sucrose solutions and stabilizes the vesicle position onto the bottom of the electroporation chamber due to the higher density of the sucrose solution in the GUV interior. The osmolarities of sucrose and glucose solutions were measured with a freezing point osmometer Osmomat 3000 (Gonotec GmbH, Germany) and matched to avoid osmotic pressure effects. The conductivities of the sucrose and glucose buffers were measured with SevenEasy Conductivity Device (Schwerzenbach, Switzerland). The results of conductivities are summarized in Table 3.

The electroporation chamber, purchased from Eppendorf (Eppendorf electrofusion chamber, Hamburg, Germany), consisted of a Teflon frame confined above and below by two glass plates through which observation is possible. A pair of parallel electrode wires ($92 \mu\text{m}$ in radius) is located at the lower glass at a distance of $475 \pm 5 \mu\text{m}$. The spacing between the electrodes is important for defining the field strength at the location of a selected vesicle above the floor of the chamber. Assuming that the electrodes are perfect cylinders, the distance between the electrodes right at the bottom glass is $674 \mu\text{m}$. Because the exact location of the vesicle center of mass above the glass cannot be precisely defined, a nominal gap distance of $500 \mu\text{m}$ between the electrodes is used, which may induce an error of $\sim 10 \%$ for the electric field strength. The chamber is attached to a β tech pulse generator GHT_Bi500 (β tech, l'Union, France), which generates square-wave direct current (DC) pulses. The pulse strength and duration ranges from 8 to 26V ($0.16 \pm$

Table 3

Composition and conductivity values of the vesicle internal and external solutions for the experimental conditions of Figs. 3–5.

Conductivity ratio, Λ	Concentration and conductivity of vesicle interior solution	Concentration and conductivity of vesicle exterior solution
0.08	200 mM sucrose, $4.35 \pm 0.65 \mu\text{S/cm}$	200 mM glucose and 1mM NaCl, $56.68 \pm 0.63 \mu\text{S/cm}$
0.14	200 mM sucrose, $4.35 \pm 0.65 \mu\text{S/cm}$	200 mM glucose and 0.5mM NaCl, $32.10 \pm 0.08 \mu\text{S/cm}$
1	200 mM sucrose, $4.35 \pm 0.65 \mu\text{S/cm}$	200 mM glucose, $4.31 \pm 0.35 \mu\text{S/cm}$
4.6	200 mM sucrose and 0.5mM NaCl, $33.69 \pm 0.04 \mu\text{S/cm}$	200 mM glucose, $4.31 \pm 0.35 \mu\text{S/cm}$
6.6	200 mM sucrose and 1mM NaCl, $62.46 \pm 2.46 \mu\text{S/cm}$	200 mM glucose, $4.31 \pm 0.35 \mu\text{S/cm}$

0.016 to 0.52 ± 0.052 kV/cm), and 10 to 50 ms, respectively.

An inverted microscope Zeiss Axiovert 200 (Jena, Germany) equipped with a Ph2 20x/0.4 objective is used to monitor GUVs in phase contrast mode. An ultra-high-speed digital camera v2512 (Phantom, Vision Research, New Jersey, USA) is mounted on the microscope and connected to a computer. Image sequences are acquired at 20,000 fps which corresponds to a sampling rate of 50 μ s, with resolution of 1.42 pixels/ μ m. The sample illumination is achieved with a mercury lamp. The onset of pulse application is defined as one frame (50 μ s) before visible vesicle deformation occurs. In order to compute the transmembrane potential of the vesicles in their deformed state, the image sequences of a total of 41 vesicles containing a single expanding pore are processed via a contour recognition numerical method [54] which allows us to extract the values of the long and short semi-axis of the vesicles. Pore radii are computed using a lab developed pore edge detection software, PoET based on a numerical method for image processing described in Ref. [28] with a precision of the order of 0.5 μ m.

The data are obtained with electropermeabilized giant unilamellar vesicles composed of POPC of radii ranging from 14 to 54 μ m filled with 0.2 M sucrose solution and immersed in a 0.2 M glucose solution to stabilize the vesicles osmotically and facilitate pore imaging under phase contrast microscopy. Above a critical V_m close to 1 V for tensionless vesicle membranes [17], the formation of macropores (diameter in the range 0.7–15 μ m) with lifetimes of up to a few hundreds of milliseconds is detected. The evolution of the size of a macropore can be individually observed under phase contrast microscopy by tracking the interrupted vesicle contour visualized from difference in refractive indexes between the inner sucrose and external glucose solutions, and detecting its radius using an automated method developed in [28]. As all observed pores are located at the vesicle pole ($\theta = 0$) we finally assume that $V_m = V_m(\theta = 0, t_p)$, takes a constant value in the time interval over which $\frac{dr}{dt}$ is measured, here t_p represents the time at which nucleation starts.

3.2. Computational procedure for assessing macropore size dynamics in electropermeabilized vesicles.

Our method follows the same numerical procedure as used by SNK in [15], and therefore, we take an electrostatic approach in computing the MST. We also assume that the membrane can be regarded as an electrically linear, homogeneous isotropic and continuous medium. Fig. 2 shows the 2D axisymmetric configuration comprising four domains: internal fluid, membrane, external fluid and pore, where the size of the system can be scaled in terms of the pore radius r . Dirichlet boundary conditions on top and bottom horizontal boundaries are applied, such as $V(z = 0) = 0$ V and $V(z = 40r) = 1$ V, to analyze the impact of V_m .

Within each domain, the following set of equations is solved.

$$\nabla \cdot \mathbf{J} = Q \quad (8)$$

$$\mathbf{J} = \lambda \mathbf{E}, \quad (9)$$

$$\mathbf{E} = -\nabla V \quad (10)$$

$$\mathbf{T} = \epsilon \epsilon_0 (\mathbf{E} \times \mathbf{E} - 1/2 E^2 \mathbf{z}) \quad (11)$$

where λ , ϵ , V and Q account respectively for the electrical conductivity, permittivity, electric potential and current density, whereas \mathbf{J} , \mathbf{T} , and \mathbf{E} refer respectively to the surface current density, Maxwell stress tensor, and electric field. Additionally, electric insulation boundary conditions, i.e. $\mathbf{n} \cdot \mathbf{J} = 0$, are applied on the vertical faces of the system while current conservation boundary conditions are applied to all other interfaces. The conductivity of the solution filling the pore is defined as a function of the conductivities of the internal and external solutions, and the vertical coordinate z

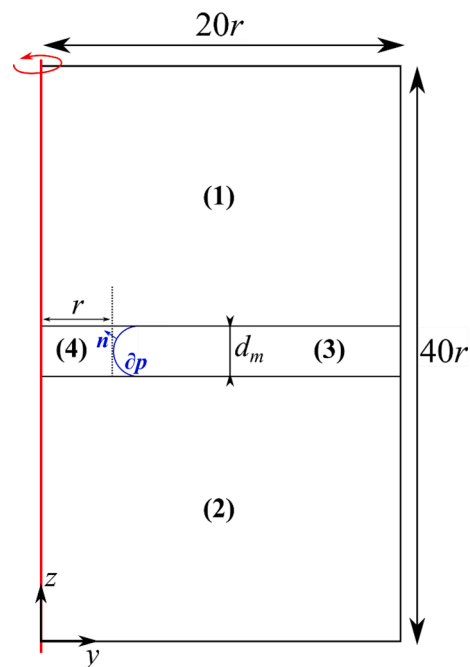


Fig. 2. Sketch (not to scale) of the numerical configuration used to compute the electrical force F_p acting on a pore during pulse application. (1), (2), (3), (4), ∂p and \mathbf{n} respectively represent the external fluid, internal fluid, membrane of thickness d_m , the pore of radius r , pore surface and the normal vector to pore surface. The red axis represents the axis of rotational symmetry.

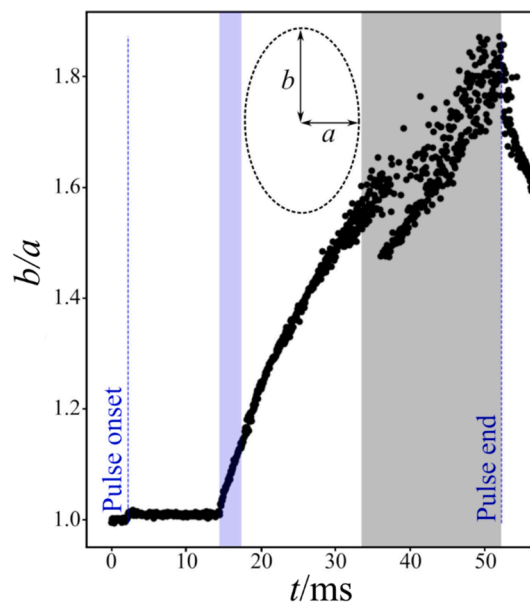


Fig. 3. Time dependence of the aspect ratio of an electrodeformed vesicle during the application of DC electric pulse (0.24 kV/cm, 50 ms). The blue dotted lines indicate the pulse onset and end, respectively. The blue shaded region corresponds to the time interval over which the pore expansion velocity (dr/dt) was considered constant in Fig. 4. The grey shaded region represents the time interval over which the pore size at the pole was too large, preventing proper detection and interpolation of the contour of the deformed vesicle with continuous ellipsoidal curve, in particular at the vesicle poles. This results in inaccurate computation of the long semi-axis b , as seen in the scatter of the data. This part of the data was not analyzed further.

$$\lambda_p = \lambda_{ext_p} - (\lambda_{ext_p} - \lambda_{in_p}) \left(\frac{z + 20r}{h} - \frac{1}{2} \right) \quad (12)$$

where λ_{ext_p} and λ_{in_p} are respectively defined as

$$\lambda_{ext_p} = \lambda_{ext} - \frac{\lambda_{ext} - \lambda_{in}}{2(1 + 2d_m/(\pi r))} \quad (13)$$

$$\lambda_{in_p} = \lambda_{in} + \frac{\lambda_{ext} - \lambda_{in}}{2(1 + 2d_m/(\pi r))} \quad (14)$$

A technical point to be made here is that Eq.(11) allows to compute the MST and the electric force F_p acting on the pore in the membrane plane which is defined as the integral of the normal component of Maxwell stresses over the surface ∂p of the pore (with reference to Fig. 2) as.

$$F_p = \iint_{\partial p} \mathbf{n} \cdot (\mathbf{T}_{(4)} - \mathbf{T}_{(3)}) n dS \quad (15)$$

As a side remark, we note that the resting potential ($dV/dt = 0$) in most polarized cells and vesicles is set to -70 mV.

From a computational perspective, the numerical analysis was performed based on finite element method computations via a cluster computer (262 GB RAM, Intel® Xeon® 2.2 GHz (48 CPUs) processor) using the COMSOL simulation package [55]. The mesh is constructed using COMSOL built-in extremely fine element size parameter setting for all domains. Eqs. (S1-S4) are solved using quadratic shape functions within triangular finite elements. Since the size of the system scales with the pore radius r ranging from 0.51 nm to 100 nm, the number of elements discretizing the pore domain is respectively of 577 up to 652, from 5541 up to 1967 elements for the membrane domain, from 94 up to 42 nodes for pore surface, and from 18,506 to 35,924 for the entire system leading to the resolution of respectively 37,315 up to 72,205 degrees of freedom which represents to computational times of respectively 21 s up to 36 s.

3.3. Matching the framework of the experimental and the numerical data

In order to shed light on the experimental validity of the foregoing results, we set a few analytical simplifications of the general theory presented in section II and restrain the theoretical frame of our analysis to micron-sized pores, which correspond to the limit of camera resolution in this study. Consequently, if we consider large pores, i.e. $r \gg 100$ nm (the minimum radius of a detectable pore being in the range of 0.5 μ m), and if we assume that membrane tension is negligible, which is expected to drop after the early stages of pore formation ($r \gg 100$ nm), and the contribution of the steric repulsion of lipid head groups (which scales as r^{-5} from Eq. (5)) is neglected, then the contribution $U(r, V_m) \approx V_m^2 f_\Lambda(r) - 2\pi\gamma$. Thus, the rate of pore expansion during pulse application is given by.

$$\frac{dr}{dt} = \frac{D}{kT} U \approx \frac{D}{kT} (V_m^2 f_\Lambda(r) - 2\pi\gamma) \quad (16)$$

Due to the large experimental variability of the pore edge tension found for POPC (and $\Lambda = 1$) in the literature, our numerical results are obtained by making use of an average value of $\gamma = 24$ pN [17–23,56].

Ultimately, our goal is to see how well SNK's model fits with the observed data. While there has been significant theoretical treatment of planar membranes (e.g. SNK [15]) there has been little study combining theoretical and experimental approaches of cell and vesicle membranes with other common shapes (spheroids, ellipsoids) during pore expansion [10,39]. Moreover, the collective nature of SKN's model, i.e. coupling of individual pores through the membrane lipid-water interfacial tension [50], is still very much unknown, and a wide variety of direct and indirect detection experiments are actively searching for evidence of post-pulse collective membrane resealing kinetics [11–12,29,31].

Fast digital imaging [17–23] offered insight into the deformation and

permeabilization of giant unilamellar vesicles subjected to electric pulses of varying strength/duration. The aspect ratio (defined as the ratio of semi-major axis b to semi-minor-axis a of the ellipsoid) of the ellipsoidal deformation for a vesicle (initially spherical) represents a reliable metric for the underlying morphology of the vesicle subjected to electric pulses as it allows to define the transmembrane potential from analytical considerations. Recently [57], there has been an increased emphasis on the role anisotropy may play in the broad set of phenomena described above. When b/a is large at elevated V_m , EP dominates, and maximum membrane deformation coincides with maximum pore aperture. The transmembrane potential for an ellipsoidal membrane can be evaluated [57] as.

$$V_m(\theta, t) = E_0 \frac{b^2 - a^2}{b - \frac{a^2}{\sqrt{b^2 - a^2}} \ln \left(\frac{b + \sqrt{b^2 - a^2}}{a} \right)} \left(\frac{a \cos(\theta)}{\sqrt{a^2 \cos^2(\theta) + b^2 \sin^2(\theta)}} \right) (1 - \exp(-(t - t_0)/\tau)) \quad (17)$$

where E_0 , t , t_0 , τ and θ respectively represent the electric field intensity, time, the time of electric pulse onset, the membrane charging time and the angle between membrane surface normal vector and the direction of the field. Using Eq. (17) for the transmembrane potential, and by defining the value of t to be the first instant at which a pore is detectable, we can now proceed with comparing theoretically predicted pore expansion rates with experimentally obtained data.

As an illustrative example, Fig. 3 shows the aspect ratio of an electroporated vesicle with a nominal applied field strength of 0.24 kV/cm, and $\Lambda = 6.6$. The initial diameter of the vesicle was 23.2 μ m and after 50 ms, it was deformed into a prolate spheroid with $b/a = 1.8$. The maximum shape deformation is attained close to the pulse end.

4. Results and discussion

In the upper top panel of Fig. 4 we show the ED and EP of a POPC vesicle characterized by phase contrast microscopy images (the data correspond to the same vesicle shown in Fig. 3). The membrane charging stage starts with the application of the electric pulse to the initially spherical vesicle followed by several electrodeformed states of the ellipsoidal membrane along the direction of the applied field. The macropores are also visualized in the snapshots of the lower top panel using our detection software [28]. The bottom panel of Fig. 4 shows the time evolution of the pore radius following our measurement protocol [28].

The guiding principle of the analysis we propose is this: in order to unravel the impact of conductivity conditions on the rate of expansion of the macropores considered in this study, we focus on the early stages of pore growth where the assumption of a quasi-constant value of V_m is valid, and defined from Eq. (17). We generated a set of data comprising the pore expansion slopes of all porated GUVs and selected only those for which a single macropore is nucleated in the membrane (Fig. 4). Fig. 5 shows the rate of pore expansion as a function of V_m^2 . The dashed lines in Fig. 5 represent the prediction of the extended SNK model for $\frac{dr}{dt}$ at a given value of Λ . On the experimental side, the linear dependence between the rate of pore expansion with V_m^2 can be clearly seen from this graph, and more importantly these trends coincide with the theoretical predictions of Eq. (7). For all data, the error bars in Fig. 5 represent experimental error associated with estimation of the slope $\frac{dr}{dt}$ and V_m^2 intercept related to the 50 μ s time scale of camera sampling. These observations lead to two important conclusions. First, the V_m dependent energy term of the SNK model ($\Lambda = 1$ in Fig. 5) appears to fall quantitatively in the range of the experimental data presented in this study. Second, the agreement between data and experiments in Fig. 5 for the case $\Lambda \neq 1$ clearly establishes the importance of Λ in the process of pore expansion, it also suggests the existence of a symmetry in the impact of solution conductivity on pore expansion, i.e. $f_\Lambda = f_{1/\Lambda}$, which suggests

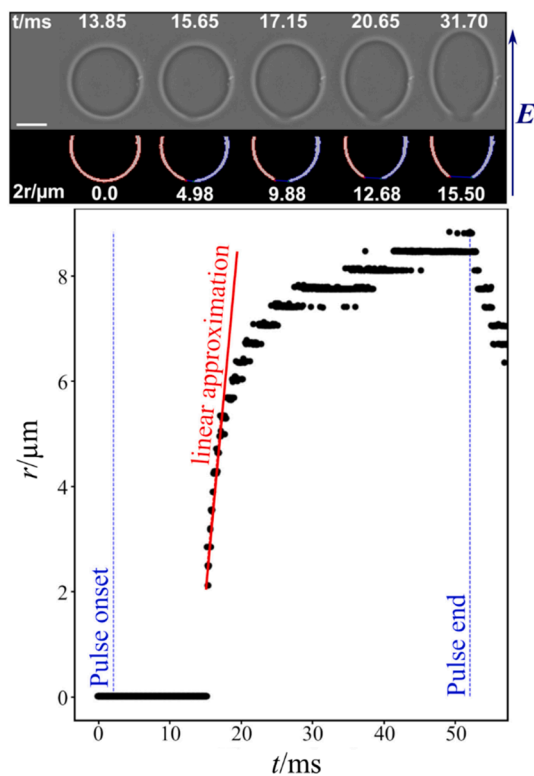


Fig. 4. Pore radius expansion as a function of time during the application of a square shaped DC electric pulse (0.24 kV/cm, 50 ms) with $\Lambda = 6.6$. The top panels show phase contrast microscopy images (upper panel) and software [28] outputs for pore radius computation (lower panel) at different times during pulse application. The scale bar represents 20 μm . The pore diameter, $2r$, and time with respect to the recording onset are indicated in each image. The graph displays the time trace of the pore radius. The blue dotted lines represent the pulse onset and end, respectively. The red line represents the linear approximation of early pore expansion.

that pore expansion does not discriminate between conditions of inverted inside vs outside vesicle media conductivity.

The observed broad range of V_m values shown in Fig. 5 can be related to the initial mechanical tension of the membrane, which is expected to lower the EP threshold of the membrane [17–23,58]. This can be also confirmed by analyzing the linear dependence (Fig. 6) of the relative increase in membrane surface area induced by the application of an electric field, $\alpha_{el} = \frac{A - A_i}{A_i}$, on the electrical tension (which is a function of V_m^2) induced in the membranes, where A and A_i respectively correspond to the surface area of the deformed vesicle and the area of a sphere of equal volume.

Based on the original studies by Helfrich [59–62], the mechanical deformation and apparent area increase of a vesicle deformed by an electric field can be presented as.

$$\alpha_{el} = \frac{8\pi\kappa}{kT} \ln\left(\frac{\sigma_{el} + \sigma_0}{\sigma_0}\right) + \frac{\sigma_{el}}{K} \quad (18)$$

where σ_0 is the initial tension of the vesicle, σ_{el} is the electrical tension induced in the membrane when the vesicle is exposed to the electric field [37,58], κ is the membrane bending stiffness (κ is on the order of 30 kT for POPC [63–64]), and K is the bulk elastic modulus of the membrane (here K is expected to be close to 0.2 N/m [64–65]). It has also been argued by Needham and Hochmuth [58] that if the electrical tension is much larger than the initial tension and if membrane incompressibility is assumed, then the total tension is.

$$\sigma = \sigma_0 + \sigma_{el} = (\alpha_0 + \alpha_{el})K \quad (19)$$

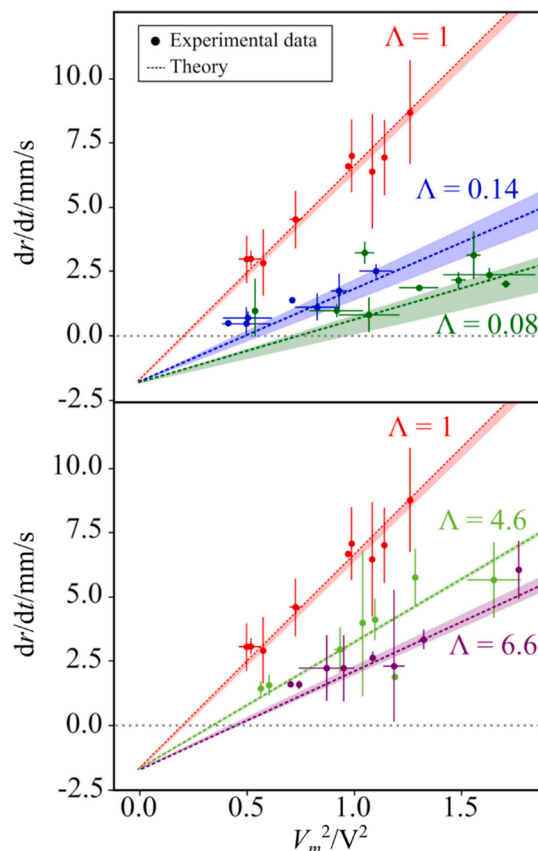


Fig. 5. Dynamics of pore expansion during electric pulse application as a function of the square of the transmembrane potential. Solid symbols show measurements on individual vesicles. For comparison, we also show the numerical results of our extension to the SNK model (dashed lines), i.e. $\frac{dr}{dt} = \frac{D}{kT} U \approx \frac{D}{kT} (V_m^2 f_\Lambda(r) - 2\pi\gamma)$, where f_Λ has been introduced to account for differences in conductivity ratio Λ displayed in different colors. For clarity, the upper panel shows results for $\Lambda \leq 1$ while the lower panel covers $\Lambda \geq 1$. See Table III for the details of the experimental conditions. The shaded regions reflect the error in f_Λ related to the measurement of Λ , and the error bars on the value of dr/dt are defined from the Frobenius norm of the diagonalized covariance matrix of $r(t)$ on the fitting interval, e.g. the “linear region” in Fig. 3. The narrow error in the case $\Lambda = 4.6$ is to be related to the low standard deviation on the measurement of conductivity conditions for this particular case as shown table II.

where

$$\sigma_{el} = \epsilon\epsilon_0 (h/2h_c^2) V_m^2 \quad (20)$$

is the electromechanical tension, ϵ is the permittivity of the membrane, ϵ_0 the vacuum permittivity, h is the total bilayer thickness, $h = 3.7$ nm, and h_c the dielectric thickness, $h_c = 2.7$ nm [58]. By contrast with Ref. [58], where the initial tension σ_0 is induced via a micropipette aspiration pressure which has for effect to increase the area of an initially unconstrained vesicle by α_0 , our vesicle preparation protocol does not permit a full control over the initial area-to-volume ratio of individual vesicles, thus resulting in vesicles with a broad range of initial tensions σ_0 in our experiments. Consequently, a decrease in the initial area-to-volume ratio increases the tension in the membrane, similarly as an isotropic swelling of the vesicle, which can be described by an initial isotropic area increase of α_0 . More significantly, the relative increase in area α_{el} induced by the electric field relies on A_i which is a function of the encapsulated volume, and thus of α_0 . For a given value of the electrical tension σ_{el} , we argue below that the relative increase in membrane area induced by the electric field can be expressed as.

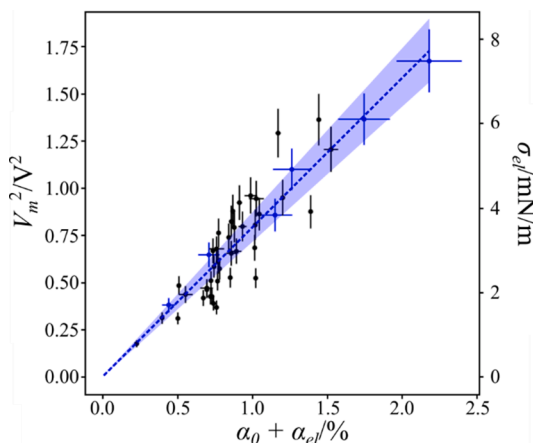


Fig. 6. V_m^2 and electrical tension σ_{el} induced in the membrane as a function of the total vesicle area increase $\alpha_{el} + \alpha_0$. The blue symbols and dashed line show the reference experimental data for which $\sigma_0 \approx 0$, while the shaded region shows the associated experimental uncertainty on the value of σ_{el} . Black dots correspond to 40 data points taken from a total of 20 electrodeformed vesicles. The slope of the blue line σ_{el} versus $\alpha_{el} + \alpha_0 \approx \alpha_{el}(\sigma_0 \approx 0)$ yields a value of the membrane stretching modulus of 0.35 ± 0.07 N/m.

$$\alpha_{el} \approx \alpha_{el}(\sigma_0 \approx 0) - \alpha_0 \quad (21)$$

where $\alpha_{el}(\sigma_0 \approx 0)$ accounts for α_{el} in the case an initially tensionless vesicle, i.e. a vesicle that encapsulates a sufficiently small volume of water so that thermal fluctuations would induce a visible flickering of its membrane surface. For that purpose, we consider the dependence of the relative area increase induced by the application of the field.

$$\alpha_{el} = \frac{A - A_i}{A_i} \quad (22)$$

on the initial isotropic area increase of α_0 . We define α_0 as

$$\alpha_0 = \frac{A_i - A_0}{A_0} \quad (23)$$

where A_i and A_0 respectively represent the initial apparent area of the vesicle and the initial apparent area of the same vesicle in the case of ($\sigma_0 = 0$). Based on this definition α_{el} can be written as

$$\alpha_{el} = \frac{A - A_i}{A_i} = \frac{\frac{A}{\alpha_0 + 1} - A_0}{A_0} = \frac{A}{A_0(\alpha_0 + 1)} - 1 \quad (24)$$

In the case of a negligible initial tension, i.e. ($\sigma_0 = 0$), we have $\alpha_0 = 0$ where.

$$\alpha_{el}(\sigma_0 = 0) = \frac{A}{A_0} - 1 \quad (25)$$

Using this relation we get.

$$\alpha_{el} = \frac{\alpha_{el}(\sigma_0 = 0) - \alpha_0}{(\alpha_0 + 1)} \approx \alpha_{el}(\sigma_0 = 0) - \alpha_0 \quad (26)$$

as $\alpha_0 \ll 1$ in our experiments.

In this context, Fig. 6 was plotted by selecting a vesicle exhibiting a flickering membrane as a reference (blue data) to compute $\alpha_{el}(\sigma_0 \approx 0)$ as a function of σ_{el} . The electrical tension was gradually increased at values above 1 mN/m in order to set our analysis within the boundaries of membrane stretching regime [63–65] (i.e. corresponding to the case $\sigma_0 \ll \sigma_{el}$), and every data point abscissa was translated by α_0 . Then, the data were fitted using the relation $\sigma_{el} = \alpha_{el}(\sigma_0 \approx 0)K$ to compute the stretching modulus K , yielding a value of 0.35 ± 0.07 N/m which is consistent with typical values reported in the literature [63–66]. The

values of the initial tensions range from 0.03 mN/m to 4.8 mN/m.

5. Concluding remarks and perspectives

To summarize, the comparison between the experimental observations of the dynamic behavior of vesicle pores under the application of an electric field with an extended version of SNK's model, showed that the conductivity ratio of the inside and the outside vesicle solution has significant and distinctive influence on the rate of change of macropore expansion in electroporabilized lipid vesicles. We also highlighted the symmetry of these effects with respect to the conductivity ratio, where our results suggest that EP efficiency should be maximized as the conductivity ratio approaches the value $\Lambda = 1$. Another novelty of our study is given by a precise and simple analytical adaptation of the SNK model, allowing to reproduce accurately the predictions of our conductivity dependent EP model.

Given these observations, it is useful to indicate the aspects in which the analysis derived in this study can capture the essence of electrodeformed and electroporabilized cells, notably the pore density dynamics in the membrane. Do the electromechanical properties of a cell membrane look like the properties of a stretched lipid bilayer? We first note that intact cell membranes contain many features not found in artificial lipid bilayers, e.g. an actin network in the cytoskeleton, whose presence was reported to prevent the formation of macropores in lipid vesicle membranes and inhibit large deformations [29]. Another feature that differs from artificial lipid bilayers is the presence of proteins in the membrane which are likely to alter the mechanical properties of the membrane [71]. Secondly, phospholipid vesicles are often used as model systems to study the electromechanical properties of living cells [39], and from the perspective of our theoretical predictions, the trends observed for large pores should be valid also for nanometric pores, which would constitute an interesting basis for the interpretation of cell EP efficiency variations induced by changes in extracellular conductivity reported in the literature [13–14]. For comparison with biological cells, Λ varies over a range of values 0.1–1 [14,39,56–57,67] and we believe that a combination of the present theory with measurements of electroporation efficiency could constitute a novel method for inferring cytoplasm conductivity. We expect our analysis will be useful to characterize the electromechanical properties of living cells, and will allow improving the current disagreement between the current state of the art numerical models and the observed impacts of Λ on electroporation efficiency [13]. A number of points still remain to be investigated, regarding the fundamental issue of the large number of small pores with a random distribution which is more relevant for realistic defective conditions in an electroporabilized cell [10–11,39]. One important question in this regard is how a SNK generalization can be implemented to deal with the intracellular mechanical changes. This connection needs to be understood in (at least) two different ways. First, there is the problem of understanding strain and stress at interfaces in-between the different phases of the cell [68–73]. And second, there is the solid phase of the cytoplasm (cytoskeleton network and macromolecular crowders) in eukaryotic cells which is known to provide structural support and mechanical stability, and play a fundamental role in controlling the rate at which the cell can be deformed [68–73]. The importance of strain engineering might prove crucial for the design of technologies like vesicle-based biosensors and artificial cells acting as drug delivery carriers. That is a formidable project, extending well beyond what is conventionally considered multiphysics [39].

Data availability

The data that support the findings of this study are available from the corresponding author upon reasonable request.

Declaration of Competing Interest

The authors declare that they have no known competing financial interests or personal relationships that could have appeared to influence the work reported in this paper.

Data availability

Data will be made available on request.

Acknowledgment

E. S. would like to thank Université de Brest for supporting this research through its PhD program. E. S. thanks the hospitality Max Planck Institute of Colloids and Interfaces, Potsdam when this work was initiated. M. A. acknowledges funding from the International Max Planck Research School on Multiscale Bio-Systems.

References

- [1] H. Isambert, Understanding the electroporation of cells and artificial bilayer membranes, *Phys. Rev. Lett.* 80 (15) (1998) 3404–3407.
- [2] K. Kinoshita, T.Y. Tsong, Formation and resealing of pores of controlled sizes in human erythrocyte membrane, *Nature* 268 (5619) (1977) 438–441.
- [3] J.C. Weaver, Y. Chizmadzhev, Theory of electroporation: a review, *Bioelectrochem. Bioenerg.* 41 (1996) 135–160.
- [4] K.A. DeBruin, W. Krassowska, Modeling electroporation in a single cell. I. Effects of field strength and rest potential, *Biophys. J.* 77 (1999) 1213–1224.
- [5] E.C. Gianulis, M. Casciola, S. Xiao, O.N. Pakhomova, A.G. Pakhomov, Electroporation by uni- or bipolar nanosecond electric pulses: The impact of extracellular conductivity, *Bioelectrochem.* 119 (2018) 10–19.
- [6] D. Shao, W.-J. Rappel, H. Levine, Computational model for cell morphodynamics, *Phys. Rev. Lett.* 105 (2010), 108104.
- [7] P. Katira, M.H. Zama, R.T. Bonnecaze, How changes in cell mechanical properties induce cancerous behavior, *Phys. Rev. Lett.* 108 (2012), 028103.
- [8] S. Sun, G. Yin, Y.K. Lee, J.T.Y. Wong, T.Y. Zhang, Effects of deformability and thermal motion of lipid membrane on electroporation: By molecular dynamics simulations, *Biochem. Biophys. Res. Commun.* 404 (2011) 684.
- [9] Z.Q. Levine, P.T. Vernier, Life cycle of an electropore: Field-dependent and field-independent steps in pore creation and annihilation, *J. Memb. Biol.* 226 (2010) 27–36.
- [10] D. Shamoon, J. Dermol-Cerne, L. Rems, M. Rebersek, T. Kotnik, S. Lasquellec, C. Brosseau, and D. Miklavčič, Assessing the electro-deformation and electroporation of biological cells using a three dimensional finite element model, *Appl. Phys. Lett.* 114 (2019) 063701(1)-063701(5).
- [11] J.T. Sengel, M.I. Wallace, Imaging the dynamics of individual electropores, *PNAS* 113 (2016) 5281–5286.
- [12] J.T. Sengel, M.I. Wallace, Measuring the potential energy barrier to lipid bilayer electroporation, *Philos. Trans. R. Soc. Lond. B Biol. Sci.* 372 (2017) 20160227.
- [13] P. Ruzgys, M. Jakutavičiūtė, I. Šatkauskienė, K. Čepurnienė, S. Šatkauskas, Effect of electroporation medium conductivity on exogenous molecule transfer to cells *in vitro*, *Sci. Rep.* 9 (2019) 1436.
- [14] V. Novickij, N. Rembiakowska, G. Staigvila, J. Kulbacka, Effects of extracellular medium conductivity on cell response in the context of sub-microsecond range calcium electroporation, *Sci. Rep.* 10 (2020) 3718.
- [15] K.C. Smith, J.C. Neu, W. Krassowska, Model of creation and evolution of stable macropores for DNA delivery, *Biophys. J.* 86 (2004) 2813–2826.
- [16] J.C. Neu, K.C. Smith, W. Krassowska, Electrical energy required to form large conducting pores, *Bioelectrochem.* 60 (2003) 107–114.
- [17] M. Yu, R.B. Lira, K.A. Riske, R. Dimova, H. Lin, Ellipsoidal Relaxation of Deformed Vesicles, *Phys. Rev. Lett.* 115 (2015), 128303.
- [18] K.A. Riske, R. Dimova, Electro-deformation and poration of giant vesicles viewed with high temporal resolution, *Biophys. J.* 88 (2005) 1143–1155.
- [19] K.A. Riske, R. Dimova, Electric pulses induce cylindrical deformations on giant vesicles in salt solutions, *Biophys. J.* 91 (2006) 1778–1786.
- [20] K.A. Riske, R.L. Knorr, R. Dimova, Bursting of charged multicomponent vesicles subjected to electric pulses, *Soft Matter* 5 (2009) 1983–1986.
- [21] R.L. Knorr, M. Staykova, R.S. Gracià, R. Dimova, Wrinkling and electroporation of giant vesicles in the gel phase, *Soft Matter* 6 (2010) 1990–1996.
- [22] T. Portet, R. Dimova, A new method for measuring edge tension and stability of lipid bilayers: effect of membrane composition, *Biophys. J.* 99 (2010) 3264–3273.
- [23] R.B. Lira, F.S.C. Leomil, R.J. Melo, K.A. Riske, R. Dimova, To close or to collapse: the role of charges on membrane stability upon pore formation, *Adv. Sci.* 8 (2021) 2004068.
- [24] R.W. Glaser, S.L. Leikin, L.V. Chernomordik, V.F. Pastushenko, A.I. Sokirko, Reversible electrical breakdown of lipid bilayers: formation and evolution of pores, *Biochim. Biophys. Acta* 940 (1988) 275–287.
- [25] L.V. Chernomordik, S.I. Sukharev, I.G. Abidor, Y.A. Chizmadzhev, Breakdown of lipid bilayer membranes in an electric field, *BBA - Biomembranes* 736 (1983) 203–213.
- [26] V.F. Pastushenko, Y.A. Chizmadzhev, V.B. Arakelyan, Electric breakdown of bilayer lipid membranes: II. Calculation of the membrane lifetime in the steady-state diffusion approximation, *J. Electroanalytical Chem. Interfacial Electrochem.* 104 (1979) 53–62.
- [27] S.A. Freeman, M.A. Wang, J.C. Weaver, Theory of electroporation of planar bilayer membranes: predictions of the aqueous area, change in capacitance, and pore-pore separation, *Biophys. J.* 67 (1994) 42–56.
- [28] F.S.C. Leomil, M. Zoccoler, R. Dimova, K.A. Riske, PoET: automated approach for measuring pore edge tension in giant unilamellar vesicles, *Bioinformatics Adv.* 1 (2021) vba037.
- [29] D.L. Perrier, A. Vahid, V. Kathavi, L. Stam, L. Rems, Y. Mulla, A. Muralidharan, G. H. Koenderink, M.T. Kreuzer, P.E. Boukany, Response of an actin network in vesicles under electric pulses, *Sci. Rep.* 9 (2019) 8151.
- [30] T. Portet, C. Favard, J. Teissié, D.S. Dean, M.P. Rols, Insights into the mechanisms of electromediated gene delivery and application to the loading of giant vesicles with negatively charged macromolecules, *Soft Matter* 7 (2019) 3872–3881.
- [31] E.B. Sozer, S. Haldar, P.S. Blank, F. Castellani, P.T. Vernier, J. Zimmerberg, Dye transport through bilayers agrees with lipid electropore molecular dynamics, *Biophys. J.* 119 (2020) 1724–1734.
- [32] J. Teissié, T.Y. Tsong, Electric field induced transient pores in phospholipid bilayer vesicles, *Biochemistry* 20 (1981) 1548–1554.
- [33] E. Tekle, R.D. Astumian, W.A. Friauf, P.B. Chock, Asymmetric pore distribution and loss of membrane lipid in electroporated DOPC vesicles, *Biophys. J.* 81 (2001) 960–968.
- [34] M.M. Sadik, J. Li, J.W. Shan, D.I. Shreiber, H. Lin, Vesicle deformation and poration under strong dc electric fields, *Phys. Rev. E* 83 (2011), 066316.
- [35] E. Sabri, S. Lasquellec, C. Brosseau, Electromechanical modeling of the transmembrane potential-dependent cell membrane capacitance, *Appl. Phys. Lett.* 117 (2020), 043701.
- [36] E. Sabri, C. Brosseau, Modelling cell membrane electrodeformation by alternating electric fields, *Phys. Rev. E* 104 (2021), 034413.
- [37] I.G. Abidor, V.B. Arakelyan, L.V. Chernomordik, Y.A. Chizmadzhev, V. F. Pastushenko, M.R. Tarasevich, Electric breakdown of bilayer lipid membranes I. The main experimental facts and their qualitative discussion, *Bioelectrochem. Bioenergetics* 6 (1979) 37–52.
- [38] J. Neu, W. Krassowska, Asymptotic model of electroporation, *Phys. Rev. E* 59 (3) (1999).
- [39] E. Goldberg, C. Suarez, M. Alfonso, J. Marchese, A. Soba, G. Marshall, Cell membrane electroporation modeling: A multiphysics approach, *Bioelectrochem.* 124 (2018) 28–39.
- [40] J. Li, W. Tan, M. Yu, H. Lin, The effect of extracellular conductivity on electroporation-mediated molecular delivery, *Biochimica et Biophysica Acta (BBA)-Biomembranes* (1828, 2013,) 461–470.
- [41] S. Movahed, D. Li, Microfluidics cell electroporation, *Microfluid Nanofluid* 10 (2011) 703–734.
- [42] S. Movahed, Y. Bazargan-Lari, F. Daneshmand, M. Mashhoodi, Numerical modeling of bi-polar (AC) pulse electroporation of single cell in microchannel to create nanopores on its membrane, *J. Membrane Biol.* 247 (2014) 1229–1237.
- [43] C. Yao, H. Liu, Y. Zhao, Y. Mi, S. Dong, Y. Lv, Analysis of dynamic processes in single-cell electroporation and their effects on parameter selection based on the finite-element model, *IEEE Trans. on Plasma Sci.* 45 (2017) 889–900.
- [44] J.L. Moran, N.N. Dingari, P.A. Garcia, C.R. Buie, Numerical study of the effect of soft layer properties on bacterial electroporation, *Bioelectrochemistry* 123 (2018) 261–272.
- [45] M.A. Chiapperino, P. Bia, C.M. Lamacchia, L. Mescia, Electroporation modelling of irregular nucleated cells including pore radius dynamics, *Electronics* 8 12 (2019) 1477.
- [46] L. Mescia, M.A. Chiapperino, P. Bia, C.M. Lamacchia, J. Gielis, D. Caratelli, Multiphysics modelling of membrane electroporation in irregularly shaped cells. 2019 Photonics & Electromagnetics Research Symposium -, 2019.
- [47] Y. Mi, J. Xu, C. Yao, C. Li, H. Liu, Electroporation modeling of a single cell exposed to high-frequency nanosecond pulse bursts, *IEEE Trans. Dielectr. Electr. Insul.* 26 (2019) 461–468.
- [48] P. Shil, S. Bidaye, P.B. Vidyasagar, Analysing the effects of surface distribution of pores in cell electroporation for a cell membrane containing cholesterol, *J. Phys. D: Appl. Phys.* 41 (2008), 055502.
- [49] X. Zhao, M. Zhang, R. Yang, Control of pore radius regulation for electroporation-based drug delivery, *Commun. Nonlinear Sci. Numer. Simulat.* 15 (2010) 1400–1407.
- [50] J. Neu, W. Krassowska, Modeling postshock evolution of large electro-pores, *Phys. Rev. E* 67 (2003), 021915.
- [51] W. Krassowska, P.D. Filev, Modelling electroporation in a single cell, *Biophys. J.* 92 (2007) 404–417.
- [52] M.I. Angelova, D.S. Dimitrov, Liposome electroformation, *Faraday Discuss. Chem. Soc.* 81 (1986) 303–311.
- [53] R. Dimova, Giant vesicles and their use in assays for assessing membrane phase state, curvature, mechanics, and electrical properties, *Ann. Rev. Biophys.* 48 (2019) 93–119.
- [54] R.S. Gracià, N. Bezlyepkina, R.L. Knorr, R. Lipowsky, R. Dimova, Effect of cholesterol on the rigidity of saturated and unsaturated membranes: fluctuation and electrodeformation analysis of giant vesicles, *Soft Matter* 6 (2010) 1472–1482.
- [55] COMSOL Multiphysics version 6.0.
- [56] G.B. Melikyan, N.S. Matinyan, V.B. Arakelian, The influence of gangliosides on the hydrophilic pore edge line tension and monolayer fusion of lipid membranes, *Biochim. Biophys. Acta.* 1030 (1990) 11–15.

- [57] T. Kotnik, G. Pucihar, and D. Miklavčič, "The cell in the electric field," in *Clinical Aspects of Electroporation*, in: S. T. Kee, J. Gehl, E. W. Lee (Eds.) (Springer Verlag, 2011), 219-43.
- [58] D. Needham, R.M. Hochmuth, "Electro-mechanical permeabilization of lipid vesicles. Role of membrane tension and compressibility," *Biophys. J.* 55 (1989) 1001-1009.
- [59] W. Helfrich, "Elastic properties of lipid bilayers-theory and possible experiments," *Z. Naturforsch. A* 28c (1973) 693-703.
- [60] W. Helfrich, "Blocked lipid exchange in bilayers and its possible influence on shape of vesicles," *A* 29c, 510-515 (1974).
- [61] W. Helfrich, "Steric interaction of fluid membranes in multilayer systems," *Z. Naturforsch. A* 33 (1978) 305-315.
- [62] W. Helfrich, R.M. Servuss, "Undulations, steric interaction and cohesion of fluid membranes," *Nuovo Cimento Soc. Ital. Fis D* 3 (1984) 137-151.
- [63] R. Dimova, "Recent developments in the field of bending rigidity measurements on membranes," *Adv. Coll. Interf. Sci.* 208 (2014) 225-234.
- [64] E. Evans, W. Rawicz, "Entropy-driven tension and bending elasticity in condensed-fluid membranes," *Phys. Rev. Lett.* 64 (1990) 2094-2097.
- [65] J. Henriksen, A.C. Rowat, E. Brief, Y.W. Hsueh, J.L. Thewalt, M.J. Zuckermann, J. H. Ipsen, "Universal behavior of membranes with sterols," *Biophys. J.* 90 (2006) 1639-1649.
- [66] W. Rawicz, B.A. Smith, T.J. McIntosh, S.A. Simon, E. Evans, "Elasticity, strength, and water permeability of bilayers that contain raft microdomain-forming lipids," *Biophys. J.* 94 (2008) 4725-4736.
- [67] M. Bloom, E. Evans, O.G. Mouritsen, "Physical properties of the fluid lipid-bilayer component of cell membranes: a perspective," *Q. Rev. Biophys.* 24 (1991) 293-397.
- [68] M. Simeonova, J. Gimsa, "The influence of the molecular structure of lipid membranes on the electric field distribution and energy absorption," *Bioelectromagnetics* 27 (2006) 652-666.
- [69] Z. Al-Rekabi, S. Contera, "Multifrequency AFM reveals lipid membrane mechanical properties and the effect of cholesterol in modulating viscoelasticity," *Proc. Natl. Acad. Sci.* 115 (2018) 2658-2663.
- [70] P. Kramar, D. Miklavčič, "Effect of the cholesterol on electroporation of planar lipid bilayer," *Bioelectrochem.* 144 (2022), 108004.
- [71] E. Moeendarbary, L. Valon, M. Fritzsche, A.R. Harris, D.A. Moulding, A. J. Thrasher, E. Stride, L. Mahadevan, G.T. Charras, "The cytoplasm of living cells behaves as a poroelastic material," *Nature Mat.* 12 (2013) 253-261.
- [72] P. Deng, Y.-K. Lee, T.-Y. Zhang, "A nonlinear electro-mechanobiological coupling model for electropore expansion in cell electroporation," *J. Phys. D-Appl. Phys.* 47 (2012), 445401.
- [73] P. Deng, Y.-K. Lee, R. Lin, T.-Y. Zhang, "Nonlinear electromechanical behavior of cell membrane during electroporation," *Appl. Phys. Lett.* 101 (2012), 053702.